

Critical scaling near the yielding transition in granular media

Abram H. Clark,¹ Mark D. Shattuck,² Nicholas T. Ouellette,³ and Corey S. O'Hern^{1,4,5}

¹*Department of Mechanical Engineering and Materials Science,
Yale University, New Haven, Connecticut 06520, USA*

²*Benjamin Levich Institute and Physics Department,
The City College of the City University of New York, New York, New York 10031, USA*

³*Department of Civil and Environmental Engineering,
Stanford University, Stanford, California 94305, USA*

⁴*Department of Physics, Yale University, New Haven, Connecticut 06520, USA*

⁵*Department of Applied Physics, Yale University, New Haven, Connecticut 06520, USA*

(Dated: September 1, 2022)

We show that the yielding transition in granular media displays second-order critical-point scaling behavior. We carry out discrete element simulations in the overdamped limit for frictionless, purely repulsive spherical grains undergoing simple shear at fixed applied shear stress Σ in two and three spatial dimensions. Upon application of the shear stress, the systems, which were originally isotropically prepared, search for a mechanically stable (MS) packing that can support the applied Σ . We measure the strain γ_{ms} before each system finds such an MS packing and stops. We show that the density of MS packings ($\propto \gamma_{\text{ms}}^{-1}$) obeys critical scaling with a length scale ξ that diverges as $|\Sigma - \Sigma_c|^{-\nu}$, where $\nu \approx 1.5$. Above the yield stress ($\Sigma > \Sigma_c$), no MS packings that can support Σ exist in the infinite-system limit. The MS packings obtained by shear possess an anisotropic fabric and loading of grain-grain contacts. In finite systems, when $\Sigma > \Sigma_c$, MS packings are characterized by a normal stress difference that also obeys critical scaling. These results shed light on granular rheology, shear jamming, and avalanches, which display nontrivial system-size dependence near yielding.

Granular materials are composed of macroscopic grains that interact via dissipative contact forces. They are athermal, and thus the constituent grains do not move in the absence of external forces. Granular media possess a nonzero yield stress, below which they are solid-like and above which they flow. Other particulate, yield-stress materials include foams [1], emulsions [2], and colloidal glasses [3] and gels [4]. Although these systems possess a range of other interactions, steric repulsion among particles often plays a dominant role in determining the system's mechanical response.

Yield and flow of granular media are controlled by the ratio $\Sigma = \tau/p$ of the applied shear stress τ to the pressure p , where p is small compared to the stiffness of grains [5, 6]. In general, grains always move in response to applied forces [7–9]. When the applied stress is above the yield stress ($\Sigma > \Sigma_c$), grains flow indefinitely, while for stresses below the yield stress ($\Sigma < \Sigma_c$) grains move temporarily until finding a nearby mechanically stable (MS) packing. For frictionless grains, MS packings generated via shear are not characterized by changes in the packing fraction ϕ [9], as in the typical jamming scenario [10–13]. Even with friction, after an initial transient regime, ϕ is similar between sheared [5] and compressed [14, 15] MS packings, suggesting that contact structure, not ϕ , plays a dominant role in determining Σ_c . Thus, Σ_c represents the shear stress above which MS packings no longer exist in the infinite-system limit. However, accurately determining this value is challenging, since the dynamics at $\Sigma \sim \Sigma_c$ are often temporally heterogeneous and spatially cooperative [16–21].

In this Letter, we show that the density of MS packings for sheared frictionless granular systems vanishes for $\Sigma > \Sigma_c \approx 0.1085$ according to second-order critical scaling with a diverging length scale $\xi \propto |\Sigma - \Sigma_c|^{-\nu}$, where $\nu \approx 1.5$. For $\Sigma > \Sigma_c$, MS packings exist for finite systems of characteristic size L , but these states vanish as L/ξ increases. For $\Sigma < \Sigma_c$, large systems ($L > \xi$) are equivalent to uncorrelated compositions of small systems. MS packings at finite Σ are characterized by anisotropy in both the stress and contact fabric tensors, and for $\Sigma > \Sigma_c$ we observe a normal stress difference that also obeys critical scaling. Our results may help to explain recent studies [21–25] showing that accurately modeling granular flows requires a cooperative length scale that grows as a power law in $\Sigma - \Sigma_c$. Moreover, our results are relevant to a broad range of amorphous solids, where second-order critical scaling has been observed near yielding [3, 26–28].

We use discrete element method simulations in two (2D) and three (3D) spatial dimensions to apply stress-controlled simple shear to systems composed of frictionless bidisperse disks in 2D (2:1 by number with size ratio 1:1.4) and spheres in 3D (2:1 by number with size ratio 1:1.2) in the overdamped limit. We show the results for 3D in the main text, and the corresponding results for 2D are provided in the Supplemental Material. In Fig. 1 (a), we show a schematic of our simulations. The lateral directions x and z (z is not present in 2D) are periodic with nondimensional length $L = l/D$, where l is the length of the box edge and D is the small grain diameter. We study $N = L^3$ grains (from $L = 3$, $N = 27$ to $L = 12$, $N = 1728$) that interact via purely repulsive, lin-

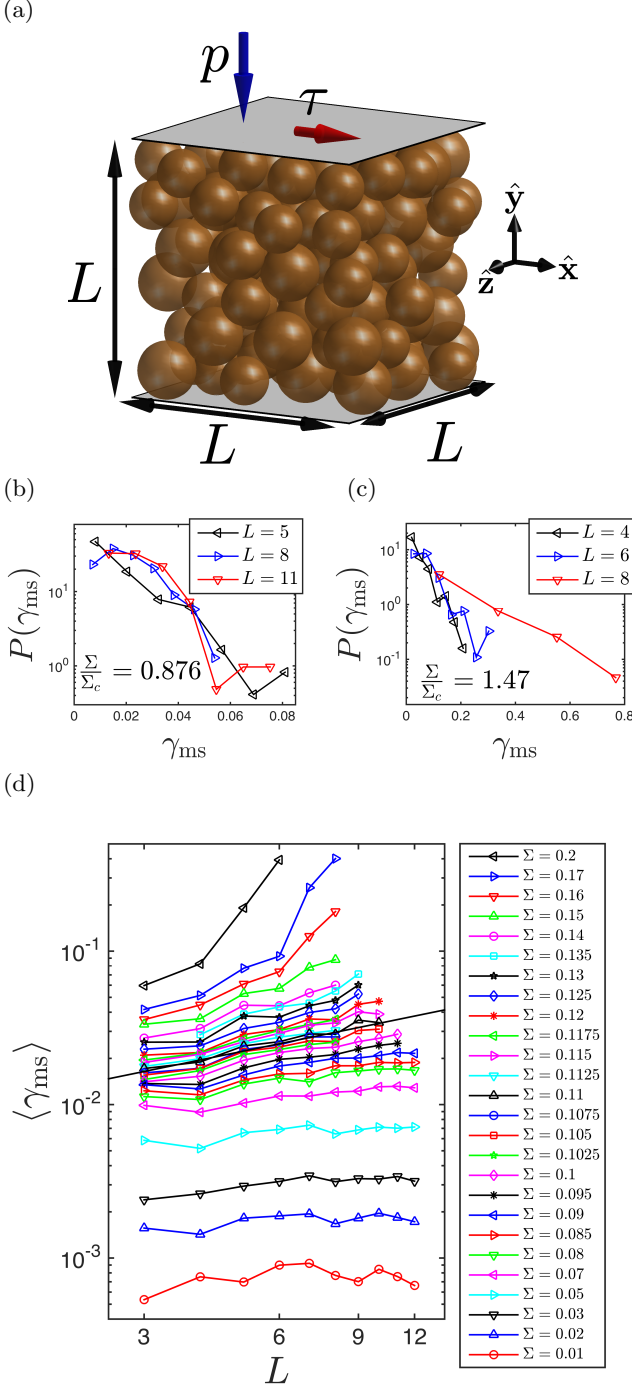


FIG. 1. (a) A schematic of the simulation procedure with the x -, y -, and z -directions indicated. We first create MS packings under only a fixed normal force per area $-p\hat{y}$. We then apply a shear force per area $\tau\hat{x}$ and search for an MS packing at a given $\Sigma = \tau/p$ and nondimensional length $L = l/D$, where l is the box edge length and D is the small grain diameter. (b-c) Probability density functions $P(\gamma_{\text{ms}})$ for the strain γ_{ms} between the initial and final MS packings for (b) $\Sigma < \Sigma_c$ and (c) $\Sigma > \Sigma_c$ and several system sizes. (d) The average strain $\langle \gamma_{\text{ms}} \rangle$ between initial and final MS packings plotted versus L over a range of Σ , where $\Sigma_c \approx 0.1085$. The solid black line shows $\langle \gamma_{\text{ms}} \rangle \propto L^{0.6}$.

ear spring forces with a characteristic stiffness K . We set $K > 10^3 p/D$ and apply viscous drag forces proportional to the velocity with damping coefficient $B > 5\sqrt{mpD}$, where m is the grain mass, to the top plate and to each grain. With these parameter values, the simulations are in the limits of large grain stiffness and low inertial number [5, 6, 22]. The top plate consists of a grid of rigidly connected small particles with gaps that are small enough to prevent bulk particles from passing through the top plate, but the plate surface is sufficiently rough to prevent slip. A no-slip condition is also maintained at the lower boundary.

We begin the simulations with grains placed sparsely throughout the domain and then apply a force per area $-p\hat{y}$ to the top plate and allow the system to compact until it reaches an MS packing. The top plate is allowed to shift laterally in the x - and z -directions, such that there are no net lateral forces on the plate in the initial MS packing at $\Sigma = 0$. We then add a shear force per area $\tau\hat{x}$ to the top plate and allow the system to evolve. The top plate can move in all coordinate directions until an MS packing is found such that $-p\hat{y}$ is balanced by a net upward force from the interior grains and $\tau\hat{x}$ is balanced by a net lateral force from the interior grains. We define the shear strain γ_{ms} as the total distance the top plate travels in the x -direction divided by the average of the initial and final y -positions of the top plate. We note that the packing fraction does not change significantly in response to the applied stress Σ as shown in the Supplemental Material.

The statistics of γ_{ms} allow us to infer the density of MS packings at each Σ and L . In Fig. 1 (b) and (c), we show the probability density function $P(\gamma_{\text{ms}})$ for two illustrative values of Σ over a range of system sizes L , obtained using 200 initial MS packings for each L . For small L above and below Σ_c , the distributions are roughly exponential, $P(\gamma_{\text{ms}}) \approx \langle \gamma_{\text{ms}} \rangle^{-1} \exp(-\gamma_{\text{ms}}/\langle \gamma_{\text{ms}} \rangle)$. This form is indicative of an underlying physical process resembling an absorption process [29], where the mean travel distance $\langle \gamma_{\text{ms}}(\Sigma, L) \rangle$ is inversely proportional to the density of absorbing MS packings as the system is sheared. Figure 1(d) shows $\langle \gamma_{\text{ms}} \rangle$ plotted versus L over a range of Σ , which shows that $\langle \gamma_{\text{ms}} \rangle$ increases monotonically with Σ . When $\Sigma \sim \Sigma_c \approx 0.1085$, then $\langle \gamma_{\text{ms}} \rangle$ increases roughly as a power law in L with exponent 0.6 (solid black line). When $\Sigma < \Sigma_c$ for large L , $\langle \gamma_{\text{ms}} \rangle$ becomes independent of L and $P(\gamma_{\text{ms}})$ develops a peak at $\gamma_{\text{ms}} > 0$. For $\Sigma > \Sigma_c$, $P(\gamma_{\text{ms}})$ remains exponential-like for large L , and $\langle \gamma_{\text{ms}} \rangle$ increases strongly with increasing L .

In Figure 2(a), we show that the curves in Fig. 1(d) can be collapsed by plotting them in terms of the scaled variables $L^{-1}/|\Sigma - \Sigma_c|^\nu$ and $\langle \gamma_{\text{ms}} \rangle^{-1}/|\Sigma - \Sigma_c|^\beta$. Thus, the density of MS states $\langle \gamma_{\text{ms}}(\Sigma, L) \rangle^{-1}$ obeys the critical

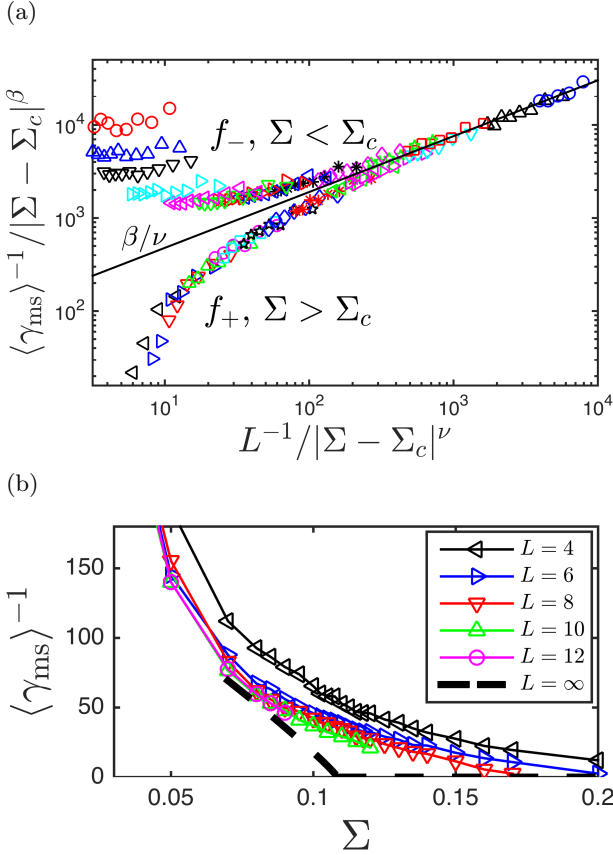


FIG. 2. (a) The same data shown in Fig. 1 (d) (with the same symbol and color conventions) collapses for $0.07 < \Sigma \leq 0.2$ when plotted using the scaled variables $\langle \gamma_{\text{ms}}(\Sigma, L) \rangle^{-1} / |\Sigma - \Sigma_c|^\beta$ and $L^{-1} / |\Sigma - \Sigma_c|^\nu$, where β and ν are scaling exponents given in Table I. (b) $\langle \gamma_{\text{ms}}(\Sigma, L) \rangle^{-1}$ versus Σ for different L . The dashed line gives the large-system limit implied by Eq. (1) and the corresponding plot in (a).

scaling relation

$$\langle \gamma_{\text{ms}}(\Sigma, L) \rangle^{-1} = |\Sigma - \Sigma_c|^\beta f_\pm \left(\frac{L^{-1}}{|\Sigma - \Sigma_c|^\nu} \right), \quad (1)$$

confirming the existence of a correlation length $\xi \propto |\Sigma - \Sigma_c|^{-\nu}$ that grows near the yielding transition. f_\pm are the critical scaling functions for $\Sigma > \Sigma_c$ and $\Sigma < \Sigma_c$, $\Sigma_c \approx 0.1085$ is the critical shear stress, and $\beta \approx 0.9$ and $\nu \approx 1.5$ are critical exponents associated with $\langle \gamma_{\text{ms}} \rangle^{-1}$ and the inverse system size L^{-1} , respectively. Near the critical point, both branches converge to a power law relation with slope $\beta/\nu \approx 0.6$, corresponding to the solid black line in Fig. 1(d). The exponents β and ν are the same in both 2D and 3D. (See Supplemental Material and Table I.) We note that $\nu \approx 1.5$ in our stress-controlled simulations differs from scaling exponents obtained from previous rate-controlled [28] and volume-controlled [12] studies of sheared granular media. Note that the scaling form breaks down sufficiently far below the critical point (*i.e.* for $\Sigma < 0.07$).

As $L^{-1}/|\Sigma - \Sigma_c|^\nu$ becomes small (*i.e.*, $L > \xi$), f_- reaches a plateau. This plateau corresponds to the characteristic behavior when $\Sigma < \Sigma_c$ and L is large shown in Fig. 1, namely the flattening of $\langle \gamma_{\text{ms}}(L) \rangle$ and the development of a peak in $P(\gamma_{\text{ms}})$ at $\gamma_{\text{ms}} > 0$. We interpret this behavior as spatial decorrelation, where large systems can be approximated as compositions of uncorrelated subsystems. When $\Sigma < \Sigma_c$ and $L > \xi$, $P(\gamma_{\text{ms}})$ is consistent with the composition of $\sim (L/\xi)^3$ exponentially distributed random variables, yielding a distribution that is peaked at $\gamma_{\text{ms}} > 0$ as in Fig. 1(b), with a mean that is independent of L/ξ . Additionally, f_+ is finite for $L < \xi$ but tends to zero for small $L^{-1}/|\Sigma - \Sigma_c|^\nu$, meaning that MS packings exist for $\Sigma > \Sigma_c$ and $L < \xi$, but these packings vanish as L grows above ξ . Figure 2 (b) shows the density of MS states $\langle \gamma_{\text{ms}}(\Sigma) \rangle^{-1}$ over a range of system sizes L , as well as the large-system limit implied by Eq. (1) and Fig. 2(a).

We quantify the structure of MS packings using the stress and contact fabric tensors,

$$\sigma_{\alpha\lambda} = \frac{1}{V} \sum_{i \neq j} r_\alpha^{ij} F_\lambda^{ij} \quad (2)$$

$$R_{\alpha\lambda} = \frac{1}{N} \sum_{i \neq j} \frac{r_\alpha^{ij} r_\lambda^{ij}}{|\mathbf{r}^{ij}|^2}. \quad (3)$$

Here, α and λ are Cartesian coordinates, $V = l^3$ is the system volume, r_α^{ij} is the α -component of the separation vector between grains i and j , and F_λ^{ij} is the λ -component of the intergrain contact force. The sum over i and j includes all pairs of contacting particles (excluding grain-wall contacts). These tensors possess eigenvalue-eigenvector pairs $\{R_k, \mathbf{R}_k\}$ and $\{\sigma_k, \boldsymbol{\sigma}_k\}$, where the index $k = 1, 2$, and 3 in 3D (or $k = 1, 2$ in 2D). The calculation of the stress and fabric tensors for a single grain is illustrated in Fig. 3 (a) and (b). Anisotropy in these tensors, *i.e.* when the eigenvalues are unequal, arises from preferential orientation and loading of grain-grain contacts [30, 31].

From continuum mechanics, force balance requires $\mathbf{s} = \boldsymbol{\sigma} \cdot \hat{\mathbf{n}}$, where $\mathbf{s} = \tau \hat{\mathbf{x}} - p \hat{\mathbf{y}}$ is the applied force per area and $\hat{\mathbf{n}} = \hat{\mathbf{y}}$ is the unit vector normal to the top surface. This implies $\sigma_{xy} = \sigma_{yx} = -\tau$, $\sigma_{yy} = p$, and $\sigma_{yz} = \sigma_{zy} = 0$, while σ_{xx} , $\sigma_{xz} = \sigma_{zx}$, and σ_{zz} are unconstrained. Fig. 3 shows the ensemble averages of the stress tensor elements obtained from simulations, and the distributions are provided in the Supplemental Material. As expected, we find that $\sigma_{xy}/\sigma_{yy} = -\Sigma$, as shown in Fig. 3 (c), and $\sigma_{yz}/\sigma_{yy} = 0$ (Supplemental Material). In addition, $\sigma_{xz}/\sigma_{yy} \approx 0$ (Supplemental Material), which is expected from symmetry, but not determined by force balance. Fig. 3 (d) shows that $R_{xy}/R_{yy} = -a\Sigma$ with $a \approx 0.4$. In Supplemental Material, we show that $R_{yz}/R_{yy} = 0$ and $R_{xz}/R_{yy} = 0$ within numerical error.

The unconstrained normal stresses σ_{xx} and σ_{zz} and the corresponding fabric tensor elements R_{xx} and R_{zz}

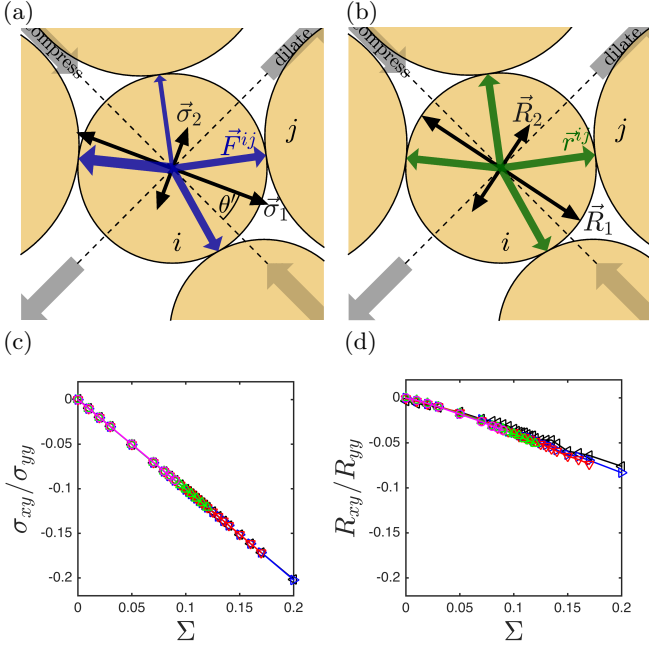


FIG. 3. (a,b) Close-up of MS packings illustrating features of the (a) stress and (b) fabric tensors in Eq. (3). Eigenvalue-eigenvector pairs from the sum over the contacts (blue and green arrows) for the center grain i are denoted with black arrows, where the magnitudes of the arrows are proportional to the eigenvalues and the directions are along the eigenvectors. The angle θ' denotes rotation of the larger eigenvector away from the compressive direction. (c,d) σ_{xy}/σ_{yy} and R_{xy}/R_{yy} plotted versus Σ , where different colors represent different system sizes L , showing $\sigma_{xy}/\sigma_{yy} = -\Sigma$ and $R_{xy}/R_{yy} = -a\Sigma$, with $a \approx 0.4$, for all L .

depend on Σ and L . We show $\sigma_{xx}/\sigma_{yy} - 1 \equiv 2\epsilon_x$ in Fig. 4 (a) and $R_{xx}/R_{yy} - 1 \equiv 2\rho_x$ in Fig. 4 (b). For $\Sigma < \Sigma_c$, ϵ_x and ρ_x begin at some finite value and tend to zero in the large-system limit. For $\Sigma > \Sigma_c$, ϵ_x and ρ_x increase with Σ . Both quantities obey critical scaling relations. For the stress anisotropy, we find

$$\epsilon_x(\Sigma, L) = |\Sigma - \Sigma_c|^\Delta h_\pm \left(\frac{L^{-1}}{|\Sigma - \Sigma_c|^\nu} \right), \quad (4)$$

as verified in Fig. 4(c). The critical exponent for ϵ_x is $\Delta \approx 1.5$, and $\Sigma_c \approx 0.1085$ and $\nu \approx 1.5$ are the same as in Eq. 1 for $\langle \gamma_{\text{ms}}(\Sigma, L) \rangle^{-1}$. In the Supplemental Material, we show that ϵ_z , ρ_x , and ρ_z also obey similar scaling relations with identical exponents in both 2D and 3D.

Thus, the ensemble-averaged stress tensor of MS packings in 3D at a given Σ is

$$\boldsymbol{\sigma} = P \begin{bmatrix} 1 + 2\epsilon_x & -\Sigma & 0 \\ -\Sigma & 1 & 0 \\ 0 & 0 & 1 + 2\epsilon_z \end{bmatrix}. \quad (5)$$

We first consider only the x - y plane, which is decoupled from z in Eq. (5), and its eigenvalue-eigenvector pairs

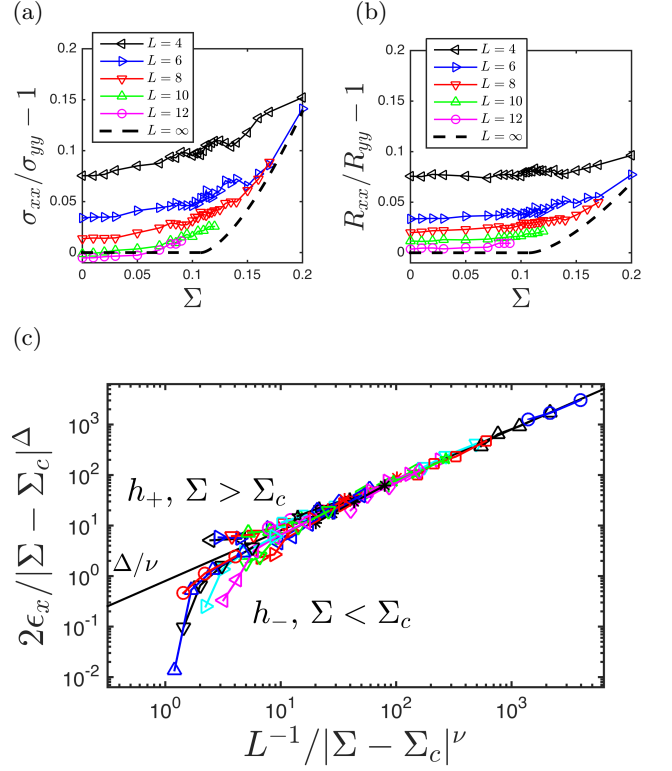


FIG. 4. (a,b) The normal anisotropies in (a) the stress tensor, $\sigma_{xx}/\sigma_{yy} - 1 \equiv 2\epsilon_x$ and (b) the fabric tensor, $R_{xx}/R_{yy} - 1 \equiv 2\rho_x$ are plotted versus Σ for different values of L . (c) The same data from panel (a), plotted as the scaled normal stress anisotropy $2\epsilon_x/|\Sigma - \Sigma_c|^\Delta$ versus scaled inverse system size $L^{-1}/|\Sigma - \Sigma_c|^\nu$. The dashed, black lines in panels (a) and (b) show the large-system limit that is implied by the collapsed data in (c) and additional data in Supplemental Material.

TABLE I. The critical stress Σ_c and critical exponents ν , β , and Δ shown in Figs. 2 (a) and 4 (c) and Eqs. (1) and (4) in 2D and 3D. Errors are estimated by varying the exponents and examining how well the data collapse in Figs. 2(a) and 4(c).

d	Σ_c	ν	β/ν	Δ/ν
2	0.1085 ± 0.005	1.5 ± 0.2	0.6 ± 0.05	1 ± 0.1
3	0.1125 ± 0.005	1.5 ± 0.2	0.6 ± 0.05	1 ± 0.1

$\{\sigma_1, \sigma_1\}$ and $\{\sigma_2, \sigma_2\}$. The internal stress anisotropy is $\Sigma_i = \tau_i/p_i$, where $p_i = (\sigma_1 + \sigma_2)/2$ and $\tau_i = (\sigma_1 - \sigma_2)$ are the internal pressure and shear stress, respectively. From the form of the stress tensor in Eq. (5), $\Sigma_i = \sqrt{\Sigma^2 + \epsilon_x^2}/(1 + \epsilon_x)$, and σ_1 is oriented at an angle that deviates from the compression direction by an angle θ' , as shown in Fig. 3 (a). An expansion of Σ_i for small ϵ_x gives $\theta' = \epsilon_x/(2\Sigma) + \mathcal{O}[(\epsilon_x/\Sigma)^3]$. Thus, when $\epsilon_x = 0$, $\Sigma_i = \Sigma$ and σ_1 and σ_2 are aligned with the compression and dilation directions, respectively. However, Σ_i is minimized by a positive, nonzero value of $\epsilon_x = \Sigma^2$ with $\Sigma_i^{\text{min}} = \Sigma/\sqrt{1 + \Sigma^2}$.

Thus, in finite-sized systems, MS packings at $\Sigma > \Sigma_c$ are characterized by a symmetry breaking, where the eigenvectors of the internal stress and fabric tensors are rotated by an angle θ' from the principal axes of the applied shear deformation. MS packings with $\theta' > 0$ may be preferable in finite systems since those with large Σ_i are likely rarer in configuration space, and $\theta' > 0$ reduces Σ_i . The excess lateral forces can also be interpreted as weak forces that buttress force chain networks. However, in the large-system limit, symmetry dictates that the fabric and stress tensors should be aligned with the axes of the applied shear deformation, and thus MS packings with nonzero θ' do not occur. We argue that the critical scaling behavior near the yield stress arises from a combination of (1) the decreasing density of MS packings at large Σ_i and (2) a propensity for the principal axes of the internal stress and fabric tensors of MS packings to be rotated relative to the axes of the applied deformation in finite-sized systems.

This research was sponsored by the Army Research Laboratory and was accomplished under Grant Numbers W911NF-14-1-0005 and W911NF-17-1-0164 (A.H.C., N.T.O., and C.S.O.). The views and conclusions contained in this document are those of the authors and should not be interpreted as representing the official policies, either expressed or implied, of the Army Research Laboratory or the U.S. Government. The U.S. Government is authorized to reproduce and distribute reprints for Government purposes notwithstanding any copyright notation herein. M.D.S. acknowledges support from the National Science Foundation Grant No. CMMI-1463455.

-
- [1] B. S. Gardiner, B. Z. Dlugogorski, G. J. Jameson, and R. P. Chhabra, "Yield stress measurements of aqueous foams in the dry limit," *J. Rheol.* **42**, 1437–1450 (1998).
 - [2] A. S. Yoshimura, R. K. Prud'homme, H. M. Princen, and A. D. Kiss, "A comparison of techniques for measuring yield stresses," *J. Rheol.* **31**, 699–710 (1987).
 - [3] P. Coussot, Q. D. Nguyen, H. T. Huynh, and D. Bonn, "Avalanche behavior in yield stress fluids," *Phys. Rev. Lett.* **88**, 175501 (2002).
 - [4] A. Boromand, S. Jamali, and J. M. Maia, "Structural fingerprints of yielding mechanisms in attractive colloidal gels," *Soft matter* **13**, 458–473 (2017).
 - [5] F. da Cruz, S. Emam, M. Prochnow, J.-N. Roux, and F. Chevoir, "Rheophysics of dense granular materials: Discrete simulation of plane shear flows," *Phys. Rev. E* **72**, 021309 (2005).
 - [6] P. Jop, Y. Forterre, and O. Pouliquen, "A constitutive law for dense granular flows," *Nature* **441**, 727–730 (2006).
 - [7] Masahiro Toiya, Justin Stambaugh, and Wolfgang Losert, "Transient and oscillatory granular shear flow," *Phys. Rev. Lett.* **93**, 088001 (2004).
 - [8] N. Xu and C. S. O'Hern, "Measurements of the yield stress in frictionless granular systems," *Phys. Rev. E* **73**, 061303 (2006).
 - [9] P.-E. Peyneau and J.-N. Roux, "Frictionless bead packs have macroscopic friction, but no dilatancy," *Phys. Rev. E* **78**, 011307 (2008).
 - [10] C. S. O'Hern, L. E. Silbert, A. J. Liu, and S. R. Nagel, "Jamming at zero temperature and zero applied stress: The epitome of disorder," *Phys. Rev. E* **68**, 011306 (2003).
 - [11] A. Donev, S. Torquato, F. H. Stillinger, and R. Connelly, "Jamming in hard sphere and disk packings," *J. Appl. Phys.* **95**, 989–999 (2004).
 - [12] P. Olsson and S. Teitel, "Critical scaling of shear viscosity at the jamming transition," *Phys. Rev. Lett.* **99**, 178001 (2007).
 - [13] M. Van Hecke, "Jamming of soft particles: geometry, mechanics, scaling and isostaticity," *J. Phys. Condens. Matter.* **22**, 033101 (2009).
 - [14] L. E. Silbert, "Jamming of frictional spheres and random loose packing," *Soft Matter* **6**, 2918–2924 (2010).
 - [15] S. Papanikolaou, C. S. O'Hern, and M. D. Shattuck, "Isostaticity at frictional jamming," *Phys. Rev. Lett.* **110**, 198002 (2013).
 - [16] P. A. Thompson, G. S. Grest, and M. O. Robbins, "Phase transitions and universal dynamics in confined films," *Phys. Rev. Lett.* **68**, 3448 (1992).
 - [17] O. Pouliquen, "Scaling laws in granular flows down rough inclined planes," *Phys. Fluids* **11**, 542–548 (1999).
 - [18] P. Jop, "Hydrodynamic modeling of granular flows in a modified couette cell," *Phys. Rev. E* **77**, 032301 (2008).
 - [19] G. Koval, J.-N. Roux, A. Corfdi, and F. Chevoir, "Annular shear of cohesionless granular materials: From the inertial to quasistatic regime," *Phys. Rev. E* **79**, 021306 (2009).
 - [20] K. Nichol, A. Zanin, R. Bastien, E. Wandersman, and M. van Hecke, "Flow-induced agitations create a granular fluid," *Phys. Rev. Lett.* **104**, 078302 (2010).
 - [21] M. Bouzid, A. Izzet, M. Trulsson, E. Clément, P. Claudin, and B. Andreotti, "Non-local rheology in dense granular flows," *Eur. Phys. J. E* **38**, 125 (2015).
 - [22] K. Kamrin and G. Koval, "Nonlocal constitutive relation for steady granular flow," *Phys. Rev. Lett.* **108**, 178301 (2012).
 - [23] M. Bouzid, M. Trulsson, P. Claudin, E. Clément, and B. Andreotti, "Nonlocal rheology of granular flows across yield conditions," *Phys. Rev. Lett.* **111**, 238301 (2013).
 - [24] D. L. Henann and K. Kamrin, "Continuum modeling of secondary rheology in dense granular materials," *Phys. Rev. Lett.* **113**, 178001 (2014).
 - [25] K. Kamrin and D. L. Henann, "Nonlocal modeling of granular flows down inclines," *Soft Matter* **11**, 179–185 (2015).
 - [26] L. Bocquet, A. Colin, and A. Ajdari, "Kinetic theory of plastic flow in soft glassy materials," *Phys. Rev. Lett.* **103**, 036001 (2009).
 - [27] S. Karmakar, E. Lerner, and I. Procaccia, "Statistical physics of the yielding transition in amorphous solids," *Phys. Rev. E* **82**, 055103 (2010).
 - [28] J. Lin, E. Lerner, A. Rosso, and M. Wyart, "Scaling description of the yielding transition in soft amorphous solids at zero temperature," *Proc. Natl. Acad. Sci.* **111**, 14382–14387 (2014).
 - [29] T. Bertrand, R. P. Behringer, B. Chakraborty, C. S. O'Hern, and M. D. Shattuck, "Protocol dependence of the jamming transition," *Phys. Rev. E* **93**, 012901 (2016).

- [30] D. Bi, J. Zhang, B. Chakraborty, and R. P. Behringer, “Jamming by shear,” *Nature* **480**, 355–358 (2011).
- [31] M. Baity-Jesi, C. P. Goodrich, A. J. Liu, S. R. Nagel, and J. P. Sethna, “Emergent $SO(3)$ symmetry of the frictionless shear jamming transition,” *J. Stat. Phys.* **167**, 735–748 (2017).